RSC Advances

ROYAL SOCIETY OF CHEMISTRY

www.rsc.org/advances

In Situ Growth of MnO_2 Nanosheets on Activated Carbon Fibers: A Low-cost Electrode for High Performance Supercapacitors

Received 00th January 20xx,
Accepted 00th January 20xx

DOI: 10.1039/x0xx00000x

www.rsc.org/

*Kai Zhu[a], Yu Wang[a], Joel A. Tang[b], Hailong Qiu[a], Xing Meng[a], Zhongmin Gao,[c] Gang Chen[a], Yingjin Wei[a], Yu Gao[a]**

Abstract MnO_2 nanosheets were successfully grown in-situ on the surface of activated carbon fibers (ACFs) via a facile microwave-assisted hydrothermal method. This environmental-friendly approach displays the advantages of low temperature, short reaction time and low cost. A series of MnO_2/ACFs composites with different MnO_2 percentages were prepared and their electrochemical performance as an electrode for supercapacitors was investigated. The 63% MnO_2 composite showed the optimal charge storage performance, remarkable rate ability, and excellent cycling capability. The enhanced electrochemical performance is attributed to the combination of good electrical conductivity of ACFs and high capacity of MnO_2. This work provides useful insight in the design and fabrication of hierarchical transition metal oxide and carbon material composite electrodes for potential applications in next generation energy storage systems.

Introduction

Considering the growing environmental problems and up-coming depletion of fossil fuel, many efforts have been devoted to the next generation of energy storage systems with high energy and power density for clean energy such as solar and wind.[1-3] Supercapacitors present their unique advantages such as high power density and long cycle stability, which shows great promise as a potential candidate for energy storage.[4-6] Generally, based on the reaction mechanism, there are two types of supercapacitors, electrochemical double layer capacitors (EDLCs) and pseudocapacitors.[7-9] For EDLCs, electrodes such as carbon materials with nanostructures (like carbon nanotubes (CNT)[10] or graphene[11, 12]) could store and release energy through nanoscopic charge separation at the electrochemical interface between the electrode and electrolyte.[13-15] However, the low capacitance of the EDLCs produces insufficient energy density to satisfy the requirements of high energy and power density for a good energy storage system. In contrast, pseudocapacitor materials, based on reversible surface redox reactions, have a significantly higher specific capacitance and energy density.[16-18]

There are numerous types of active materials being studied to be used as pseudocapacitors including RuO_2,[19, 20] NiO_x,[21, 22] TiO_2,[23-25] CoO_x,[26-28] and VO_2.[29, 30] However, many have not been adapted for commercial use due to either high production costs or low capacitances. MnO_2 materials are being intensively investigated because of their high theoretical capacitance, low cost, high natural abundance, and low environmental impact.[31-33] Unfortunately, they suffer poor electrical conductivity and slow ion transport rate, limiting the specific capacitance and charge-discharge rate.[33-35] To overcome these problems, nanostructured MnO_2 materials could be designed to effectively reduce the ion diffusion length.[36] Yan et al. prepared MnO_2 tubular nanostructures using carbon nanofibers as a sacrificial template via a hydrothermal method. The tubular MnO_2 nanostructures could achieve high capacitance (200 F/g) at current density of 5 A/g.[32] However, the template increases the cost of production. Feng et al. reported a method to produce MnO_2 nanowires, by calcination of MnOOH, without the need of a template.[37] The MnO_2 nanowires displayed a capacitance of 120 F/g and good cycling performance at a scan rate of 50 mV/s. Although the application benefits of MnO_2 supercapacitors are great, expenses and environmental impacts could be high, therefore, a low cost and greener approach is extremely necessary. An alternative approach is to combine the active materials with carbon materials such as CNT[38], graphene[39] and activated carbon[40]. Lou reported a 1D template-engaged method to grow ultrafine CuS nanoneedles on CNTs which exhibited a high capacitance of 110 F/g and excellent capacitance retaining after 1000 cycles.[38] Through a hydrothermal method, followed by two-step calcination, Mai et al. were able to synthesize a 3D architecture of cobalt oxide nanobrush-graphene@$Ni_xCo_{2x}(OH)_{6x}$ with improved electrochemical performance.[41] The combination of carbon materials and metal oxide materials not only provides an improved conductive network but also contribute towards the total capacitance similar to electrochemical double layer capacitors. However, the tedious fabrication processes and high price of carbon materials limit their practical applications. Therefore, it is highly desirable to develop a simple method to combine the MnO_2 nanomaterials with low-cost carbon electrode material for supercapacitors.

In this paper, we designed and prepared MnO_2 nanosheets in-situ grown on the surface of activated carbon fibers (ACFs) via a microwave-assisted hydrothermal process. This method is simple, fast and environmentally friendly, which would be suitable for the large-scale production. Moreover, production costs would be substantially reduced by the types of raw materials being used such as commercial potassium permanganate and activated carbon fibers prepared from abandoned polyacrylonitrile (PAN)-based precursor fibers. To the best of our knowledge, this approach has not been reported. To obtain a better electrochemical performance,

[a] *Key Laboratory of Physics and Technology for Advanced Batteries, Ministry of Education, College of Physics, Jilin University, Changchun 130012, PR China.*
[b] *Department of Chemistry, Johns Hopkins University, Baltimore MD, 21218 (USA).*
[c] *A State Key Laboratory of Inorganic Synthesis & Preparative Chemistry, Jilin University, Changchun 130012, Jilin, China.*
*E-mail: yugao@jlu.edu.cn

the content of the MnO_2 in the composite is investigated and optimized. The 63% MnO_2/ACFs composite holds a larger capacity and has a good charging rate ability which was attributed to the combination of good electrical conductivity of ACFs and high capacity of MnO_2. This work presents a possible preparation route towards high performance electrodes with low production cost and environmentally friendly production methods, which could be applicable to design other electrode materials for energy storage and transfer systems.

Experimental section

Material preparation

The abandoned PAN-based precursor fibers obtained from Jilin Petro-Chemical Company were washed completely by deionized water and dried at 120 °C for 12 h. The dried PAN-based precursor fibers were heated at 600 °C under N_2 gas flow with the speed of 10 mL/min for 1h. Then the carbonized fibers were heated up to 900 °C at a rate of 5 °C /min under N_2 gas flow and kept under CO_2 gas flow with the speed of 100 mL/min for 1h. After cooling down to room temperature, the ACFs were obtained.

The MnO_2/ACFs composite was prepared by a fast and green microwave-assisted hydrothermal method. 0.2 g of ACFs was added to a solution of $KMnO_4$ that was dispersed in deionized water and stirred for 30 min. The mixture was transferred into a 50 mL Teflon vessel and treated by microwave irradiation at 120 °C for 30 min. The final product was collected by vacuum filtration, washed with deionized water several times and dried in a vacuum oven for 24 h. Different amounts of $KMnO_4$ (0.079, 0.632, and 1.264 g) was used to vary the MnO_2 percent composition. For comparison, pure MnO_2 was prepared under the same conditions using glucose instead of activated carbon fibers

Materials characterization

Crystal structure of the sample was characterized by a Bruker D8 Advance Diffractometer instrument using Cu Kα radiation. The morphology of the materials was investigated using a JSM-6700F scanning electron microscope (SEM). Transmission electron microscopy (TEM) and high-resolution transmission electron microscopy (HRTEM) were recorded with a JEM-2200FS field emission transmission electron microscope. Gas adsorption studies were conducted on a Micromeritics ASAP2420 Accelerated Surface Area and Porosimetry system. The amount of carbon in the samples was measured by using a Vario El III elemental analyzer.

All the electrochemical properties were investigated in a three-electrode configuration cell using a film electrode as the working electrode, a platinum plate (1×1 cm^2) as the counter electrode, and a saturated calomel electrode as the reference electrode in 1 M Na_2SO_4 aqueous electrolyte. The working electrode was prepared by mixing 85 wt% of the active material, 10 wt% of carbon conductive additive, 5 wt% of PTFE as a binder. A small amount of ethanol was added to the mixture to produce a homogeneous paste. The mixture was pressed onto nickel foam current-collectors (1×4 cm^2) within an area of 1×1 cm^2 and dried in a vacuum oven at 110 °C overnight. Cyclic voltammetry (CV) and AC impedance spectroscopy measurements were conducted on a VSP multichannel potentiostatic-galvanostatic system (Bio-logic SAS, France). The galvanostatic charge-discharge measurements were performed on a Landt automatic battery tester (Wuhan, China).

Results and discussion

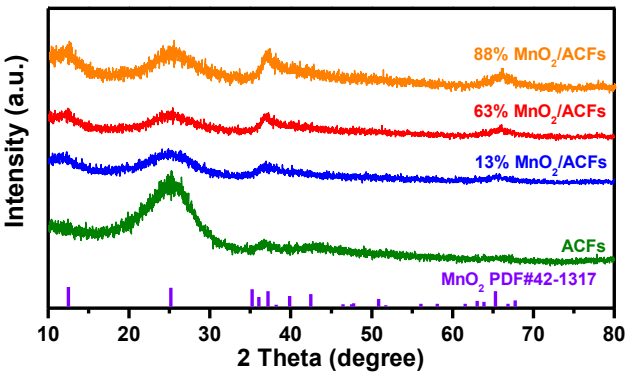

Figure 1. XRD patterns of different contents of MnO_2 and ACFs composites and pure ACFs. The vertical lines on the x-axis correspond to the standard XRD reflection of birnessite-type MnO_2.

Figure 1 displays the X-ray diffraction (XRD) pattern of as-prepared MnO_2/ACFs composite materials and pure ACFs. The broad peaks at 36.8° and 65.7° are associated with the MnO_2 nanostructures with a characteristic pattern of birnessite-type MnO_2 (PDF # 42-1317). The crystal structure of the MnO_2 nanosheet is indexed to the monoclinic crystalline phase of birnessite-type MnO_2 (space group: C2/m). The hump between 20 and 30° is caused by disorder (002) stacking layers of the ACFs. In addition, the intensity of the peak belonging to MnO_2 increases with the addition of $KMnO_4$ to the reaction, which suggests the increasing content of MnO_2 in the composites. To confirm the content of the MnO_2 in the composites, the CHN testing was performed. The content of MnO_2 in the composites is calculated to be 13%, 63%, and 88% corresponding to the addition of 0.079, 0.632, and 1.264 g $KMnO_4$, respectively. The composites with 13%, 63% and 88% MnO_2 are reported as 13% MnO_2/ACFs, 63% MnO_2/ACFs and 88% MnO_2/ACFs from here on in, respectively.

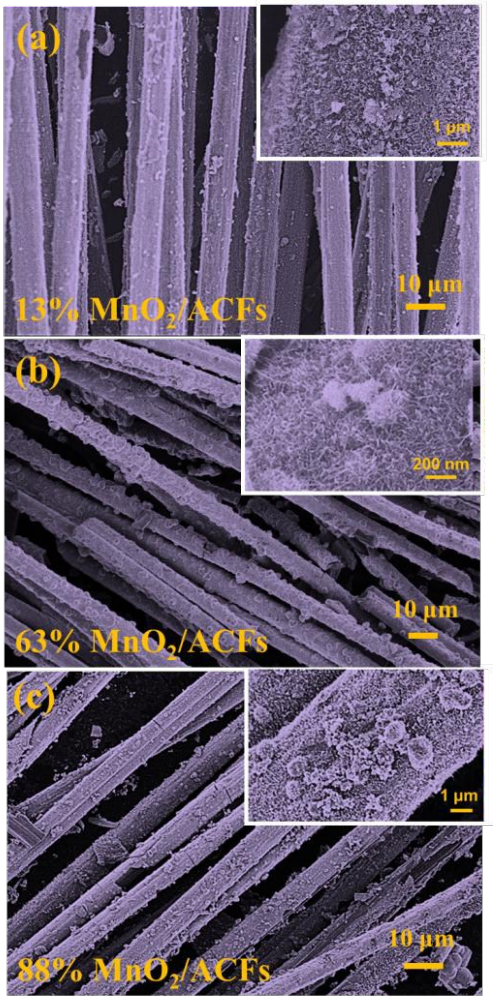

Figure 2. SEM images of (a) 13% MnO_2/ACFs, (b) 63% MnO_2/ACFs and (d) 88% MnO_2/ACFs.

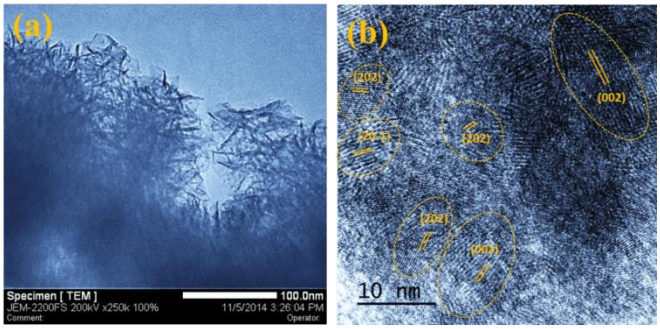

Figure 3. (a) TEM image and (b) HRTEM image of 63% MnO_2/ACFs composite.

The morphologies of the composite with different content of MnO_2 were investigated by the SEM and depicted in **Figure 2**. MnO_2 is spread across the entire surface of the ACFs, with more binding as higher concentrations of $KMnO_4$ is added. The MnO_2 nanosheets on the ACFs could be clearly seen in the **Figure 2a**. For the 63% MnO_2/ACFs, the MnO_2 completely cover the ACFs and there are some hairline cracks, which would benefit for the electrolyte soaking. However, increasing the amount of $KMnO_4$ further would lead to formation of hierarchical structure self-assembled by MnO_2 nanosheet as shown in **Figure 2b**. For the 88% MnO_2/ACFs, many MnO_2 microspheres are formed and anchor on the surface of ACFs through a self-assembling process. To further understand the

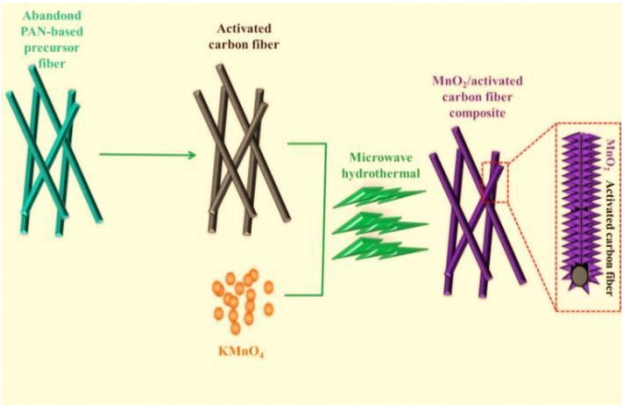

Figure 4. Schematic illustration of the synthesis route of MnO_2 and ACFs composites.

nanostructure of the MnO_2, TEM images were acquired for 63% MnO_2/ACFs and are shown in **Figure 3. Figure 3a** further confirms that the morphology of the as-prepared MnO2 material is present as nanosheets with a thickness of less than 10 nm, which is similar with previous report.[42, 43] The electronic storage of MnO2 materials is associated with the insertion of sodium ions between the layers, which is highly beneficial for ion transition during the electrochemical process.[42] The nanosheets provide a large specific surface area which is also helpful in enhancing the electrochemical performance. The HRTEM image shown in the **Figure 3b** reveals the interplane spacings of 0.189, 0.253 and 0.351 nm for the nanosheet, corresponding to the (202), (20-1), and (002) planes of MnO_2, respectively. Based on the above analysis, a formation mechanism of the composite is illustrated in **Figure 4**. The ACFs were obtained from discarded PAN-based precursor fibers, reducing its cost, through carbonization and activating processes. The ACFs are then added into a $KMnO_4$ solution. During a microwave-assisted hydrothermal reaction, $KMnO_4$ is reduced to MnO_2 and deposited on the surface of ACFs, as the following reaction proceeds:

$$MnO_4^- + 2H_2O + 3e^- \rightarrow MnO_2 + 4OH^-$$

and the MnO_2 self-assemble into the MnO_2 nanosheets. In addition, higher concentration of $KMnO_4$ leads to a greater formation of MnO_2 and the MnO_2 nanosheets would self-assemble into the microsphere with hierarchical structure. It should be noted that in this reaction only commercial $KMnO_4$, low-cost ACFs and water were used, which could reduce production cost. The reaction time is only 30 min with this facile experimental procedure due to the microwave-assisted approach. Thus, such an effortless, low-cost and green method is suitable for large-scale production.

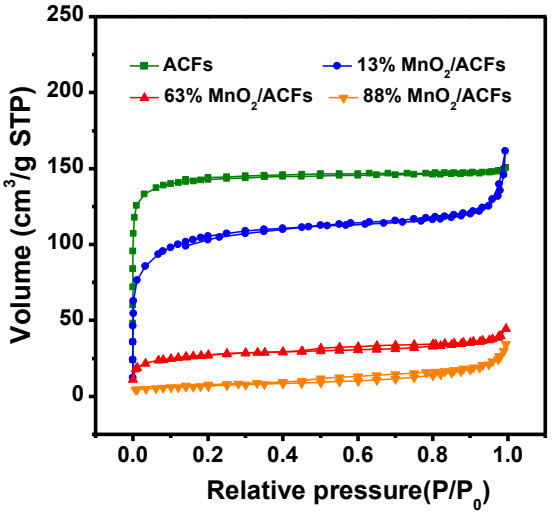

Figure 5. N_2 adsorption/desorption isotherm curves of different contents of MnO_2 and ACFs composites.

The specific surface area and pore size distribution of the samples were investigated by nitrogen adsorption-desorption isotherms and the standard multipoint Brunauer-Emmett-Teller (BET) method was used to calculate the specific surface area of the composite (**Figure 5)**. The ACFs prepared from abandoned PAN-based precursor fibers display a large surface area of 468 m^2/g. The addition of MnO_2 reduces the surface area of 13% MnO_2/ACFs, 63% MnO_2/ACFs and 88% MnO_2/ACFs to 355, 93, 24 m^2/g, respectively. This suggests that the MnO_2 on the surface of the ACFs could block the pores affecting the electrochemical performance. In addition, by increasing the MnO_2 content, the surface area of the composite reduces which results in poor connection between the electrode and electrolyte.[31]

To investigate the electrochemical performance of the composite, ACFs with different contents of MnO_2 and pure MnO_2 were tested as a supercapacitor electrode using CV while employing a scan range of 1 mV/s to 10 mV/s. At 1 mV/s, the CV curves of every sample exhibit good rectangular and symmetric shapes as shown in **Figure 6a**, which suggests the materials display fast reversible Faradic reaction and ideal capacitive behaviour.[34] The specific capacitances of the samples were calculated from the CV curves according the equation (1):

$$C=Q/(\Delta V \times m) \quad (1)$$

where C is the specific capacitance, Q is the average charge during the charge-discharge process, ΔV is the potential voltage and m is the mass of the active materials. ACFs have a capacitance of 64 F/g in the Na_2SO_4 electrolyte solution. As the MnO_2 content increases, the capacitance becomes larger with the largest capacitance of 220 F/g being measured for pure MnO_2. When the scan rate becomes 10 mV/s, the CV curves have nearly a symmetrical rectangular shape as shown in **Figure 6b**. The 63% MnO_2/ACFs shows the largest capacitance of 120 F/g, which is attributed to the unique composite structure: MnO_2 contributes a large capacitance and ACFs provides a "rapid track" for the electronic transition.[44] Thus, too much MnO_2 or ACFs would result in electrochemical performance degradation, suggesting that the 63% MnO_2/ACFs composition provides an optimal balance for a superconductor.

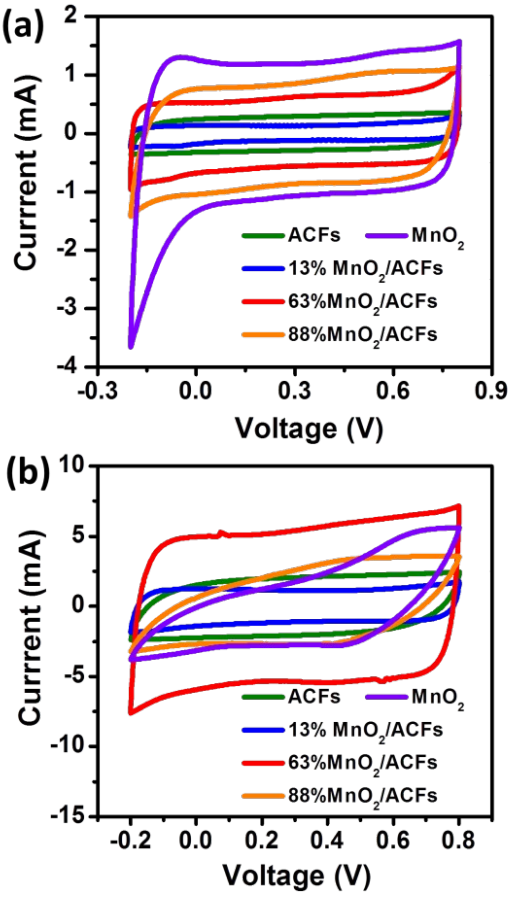

Figure 6. CV curves of different contents MnO_2 and ACFs composite under scan rate of (a) 1 mV/s and (b) 10 mV/s.

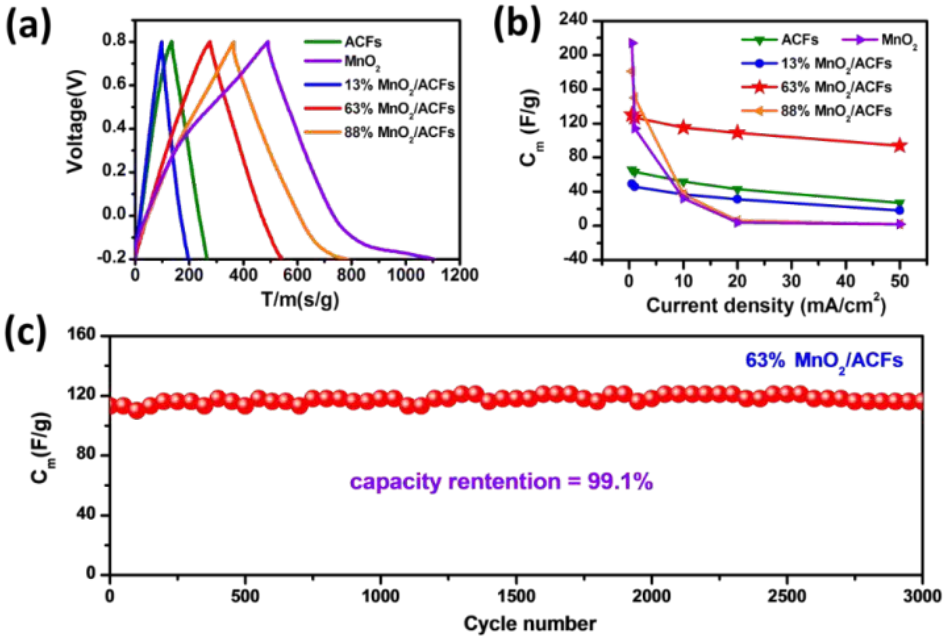

Figure 7. (a) Discharge-charge profiles of different contents of MnO_2 and ACFs composites; (b) comparison of specific capacitances of different contents of MnO_2 and ACFs composites at different scan rates; (c) cycling performance of 63% MnO_2/ACFs at scan rate of 10 mA/cm^2.

	Electrolyte	Voltage	Current density	Capacitance	Cycling number	Capacitance retention
Graphene oxide-MnO_2[45]	1 M Na_2SO_4	0-1 V	200 mA/g	197 F/g	1000	84.1%
MnO_2@carbon[46]	6 M KOH	-1-0 V	5 mV/s	123.5 F/g	--	--
MnO_2/CNT[47]	0.5 M Na_2SO_4	-0.1-0.8 V	5 A/g	90 F/g	2000	90.1%
Au-MnO_2/CNT[48]	0.1 M Na_2SO_4	0-0.8 V	6.6 A/g	68 F/g	1000	97.0%
MnO_2/mesoporous carbon[49]	2 M KCl	0-1 V	5 mV/s	173 F/g	1000	92.5%
Graphene wrapped MnO_2[50]	1 M Na_2SO_4	0-1 V	10 mV/s	170 F/g	1000	82.3%
MnO_2-CNT/graphene[51]	1 M Na_2SO_4	0-0.9 V	2 A/g	123 F/g	1300	70%
MnO_2/ACFs (this work)	**1 M Na_2SO_4**	**-0.2-0.8 V**	**10 mA/cm^2**	**117 F/g**	**3000**	**99.1%**

Table1 The electrochemical performance for reported MnO_2 and carbon materials composite.

To get more information about the electrochemical performance of the composite as an electrode for supercapacitors, galvanostatic charge/discharge measurements were carried out in 1M Na_2SO_4 between -0.2 and 0.8 V at a current density of 0.5 mA/cm^2. As illustrated in **Figure7a** all samples present smooth charge-discharge curves and the capacitance of the samples were calculated according to equation (2) as follows:

$$C = I \times \Delta t / (\Delta V \times m) \quad (2)$$

where I is the constant discharge current, Δt is the discharge time, and ΔV is the potential drop during the discharge and m is the mass of composite or the active materials. The pure MnO_2 has the largest capacitance and as the content of MnO_2 decreases so does the capacitance, which is consistent with the results of the CV. It should be noticed that the capacitance of 13% MnO_2/ACFs is lower than that of ACFs. The MnO_2 on the surface of ACFs blocks the pores, greatly reducing the double layer capacity value of the ACFs.[52] Thus low content of MnO_2 results in a poor electrochemical performance. To further investigate the rate capability, the materials were tested

under different current densities as shown in **Figure 7b**. Although pure MnO_2 and 88% MnO_2/ACFs display a large capacitance at small current density, when the current density increases to 20 or 50 mA/cm^2, the capacitance falls to almost zero. The poor rate ability is potentially caused by the low conductivity of the MnO_2 which limits the electron transition in such a process. On the contrary, the 63% MnO_2/ACFs shows a much better rate ability. Even at a high current density of 50 mA/cm^2, the capacitance of 94 F/g is maintained. The capable rate ability should attribute to the high conductivity of the ACFs, which could enhance the electron transition during the charge and discharge process. Although ACFs also exist in the composite 83% MnO_2/ACFs, part of MnO_2 would not make contact with the ACFs due to the abundant amount of MnO_2, which hinders the electronic transition in the composite. Based on the above results, the content of 63% MnO_2 should be a better choice, which could provide both high capacitance and remarkable rate ability. Furthermore, cycling stability of 63% MnO_2/ACFs was investigated, which is a critical parameter for high performance supercapacitors. **Figure 7c** presents the cycling performance of the 63% MnO_2/ACFs at a current density of 10 mA/cm^2. The material displays a remarkable capacitance of 117 F/g. After 3000 cycles there is almost no fading in the capacitance of the electrode, maintaining a constant capacitance of 116 F/g. In addition, as-prepared MnO_2/ACFs composites present a competitive electrochemical performance compared with previously reported MnO_2/carbon material (e.g. CNT and graphene) composites as shown in the **Table 1**. The MnO_2/ACFs composite shows a better cycling performance than other composite. Thus, this suggests that the 63% MnO_2/ACFs is a capable and promising candidate for a high performance electrode for large scale energy storage.

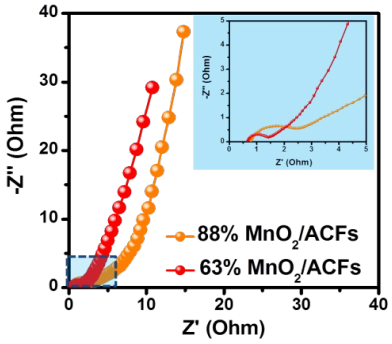

Figure 8. AC impedance spectroscopy of supercapacitors with 63% and 88% MnO2/ACFs composite electrode.

Moreover, AC impedance spectroscopy was used to gain a better understanding of the high capacitance at high current density of 63% and 88% MnO_2/ACFs (Figure 8). The samples present a typical impedance spectrum with three distinct regions: (i) a loop in the high frequencies attributed to the charge-transfer resistance; (ii) a line with a slope close to 45° in the intermediate frequency region, which is related to ion diffusion into the electrode interface; and (iii) an almost vertical line at low frequency, which reflects the purely capacitive characteristic. It is clearly shown that the charge-transfer resistance of the 63% MnO_2/ACFs (~0.8 Ω) is smaller than that of 88% MnO_2/ACFs (~1.7 Ω). Increased content of MnO_2 would decrease the connected area between the MnO_2 and ACFs, which would result in a larger charge-transfer resistance. Therefore, 63% MnO_2/ACFs show a better rate ability than 88% MnO_2/ACFs.

Conclusion

In summary, a low-cost MnO_2 and ACFs composites were designed and fabricated through a facile, green and fast microwave-assisted hydrothermal process. Different contents of MnO_2 nanosheets in-situ grown on ACFs were synthesized and investigated as an electrode for supercapacitors. The composite with 63% MnO_2 shows the best electrochemical performance including enhanced capacitance, excellent cycling ability, and remarkable rate capability. The significant improvement should attribute to unique 1D hierarchical nanostructure, in which MnO_2 nanosheets provide high capacitance and ACFs enhance the electronic transition in the composite. Thus MnO_2/ACFs could be considered as a promising capable electrode for high performance supercapacitors. In addition, this work provides useful insight in design and fabrication of hierarchical transition metal oxide and carbon materials composite electrodes for potential applications in next generation energy storage systems.

Acknowledgements

This research was financially support by the Science & Technology Department of Jilin Province (No. 20140520093JH and NO. 20150312002ZG), Open Project of State Key Laboratory of Superhard Materials (Jilin University, No. 201513), State Major Scientific Instrument and Equipment Development of China (No. 2012YQ24026407), and China Education Resource System (No. CERS-1-3).

Notes and references

‡ Footnotes relating to the main text should appear here. These might include comments relevant to but not central to the matter under discussion, limited experimental and spectral data, and crystallographic data.

1. M. F. El-Kady and R. B. Kaner, *Nat Commun*, 2013, **4**, 1475.
2. S. Kondrat, C. Perez, V. Presser, Y. Gogotsi and A. Kornyshev, *Energ Environ Sci*, 2012, **5**, 6474-6479.
3. S. Wu, W. Chen and L. Yan, *J Mater Chem A*, 2014, **2**, 2765-2772.
4. Y. Zhao, J. Liu, Y. Hu, H. Cheng, C. Hu, C. Jiang, L. Jiang, A. Cao and L. Qu, *Adv Mater*, 2013, **25**, 591-595.
5. J. Ren, L. Li, C. Chen, X. Chen, Z. Cai, L. Qiu, Y. Wang, X. Zhu and H. Peng, *Adv Mater*, 2013, **25**, 1155-1159.
6. Q. Wang, J. Xu, X. Wang, B. Liu, X. Hou, G. Yu, P. Wang, D. Chen and G. Shen, *ChemElectroChem*, 2014, **1**, 559-564.
7. L. F. Chen, Z. H. Huang, H. W. Liang, Q. F. Guan and S. H. Yu, *Adv Mater*, 2013, **25**, 4746-4752.

8. C. Zheng, C. Cao, Z. Ali and J. Hou, *J Mater Chem A*, 2014, **2**, 16467-16473.
9. B. You, L. Wang, N. Li and C. Zheng, *ChemElectroChem*, 2014, **1**, 772-778.
10. B. You, L. Wang, L. Yao and J. Yang, *Chem Commun*, 2013, **49**, 5016-5018.
11. P. Chen, J.-J. Yang, S.-S. Li, Z. Wang, T.-Y. Xiao, Y.-H. Qian and S.-H. Yu, *Nano Energy*, 2013, **2**, 249-256.
12. R. R. Salunkhe, S. H. Hsu, K. C. Wu and Y. Yamauchi, *ChemSusChem*, 2014, **7**, 1551-1556.
13. D. H. Seo, S. Yick, Z. J. Han, J. H. Fang and K. K. Ostrikov, *ChemSusChem*, 2014, **7**, 2317-2324.
14. L. Sun, Y. Fu, C. Tian, Y. Yang, L. Wang, J. Yin, J. Ma, R. Wang and H. Fu, *ChemSusChem*, 2014, **7**, 1637-1646.
15. H. Wang, Z. Li and D. Mitlin, *ChemElectroChem*, 2014, **1**, 332-337.
16. Y. Qian, R. Liu, Q. Wang, J. Xu, D. Chen and G. Shen, *J Mater Chem A*, 2014, **2**, 10917-10922.
17. Y. Bai, M. Du, J. Chang, J. Sun and L. Gao, *J Mater Chem A*, 2014, **2**, 3834-3840.
18. H. Pang, S. J. Ee, Y. Dong, X. Dong and P. Chen, *ChemElectroChem*, 2014, **1**, 1027-1030.
19. P. Wang, H. Liu, Q. Tan and J. Yang, *RSC Adv*, 2014, **4**, 42839-42845.
20. Z. Zhou, Y. Zhu, Z. Wu, F. Lu, M. Jing and X. Ji, *RSC Adv*, 2014, **4**, 6927-6932.
21. J. Xu, Q. Wang, X. Wang, Q. Xiang, B. Liang, D. Chen and G. Shen, *ACS Nano*, 2013, **7**, 5453-5462.
22. X. Wu, Y. Zeng, H. Gao, J. Su, J. Liu and Z. Zhu, *J Mater Chem A*, 2013, **1**, 469-472.
23. H. Li, Z. Chen, C. K. Tsang, Z. Li, X. Ran, C. Lee, B. Nie, L. Zheng, T. Hung and J. Lu, *J Mater Chem A*, 2014, **2**, 229-236.
24. D. Pan, H. Huang, X. Wang, L. Wang, H. Liao, Z. Li and M. Wu, *J Mater Chem A*, 2014, **2**, 11454-11464.
25. C. Huang, N. P. Young and P. S. Grant, *J Mater Chem A*, 2014, **2**, 11022-11028.
26. C. Xiang, M. Li, M. Zhi, A. Manivannan and N. Wu, *J Power Sources*, 2013, **226**, 65-70.
27. R. Rakhi, W. Chen, M. Hedhili, D. Cha and H. Alshareef, *ACS Appl Mater Interfaces*, 2014, **6**, 4196-4206.
28. Y. G. Zhu, Y. Wang, Y. Shi, J. I. Wong and H. Y. Yang, *Nano Energy*, 2014, **3**, 46-54.
29. H. Wang, H. Yi, X. Chen and X. Wang, *J Mater Chem A*, 2014, **2**, 1165-1173.
30. M. Yu, Y. Zeng, Y. Han, X. Cheng, W. Zhao, C. Liang, Y. Tong, H. Tang and X. Lu, *Adv Funct Mater*, 2015.
31. W. Li, K. Xu, B. Li, J. Sun, F. Jiang, Z. Yu, R. Zou, Z. Chen and J. Hu, *ChemElectroChem*, 2014, **1**, 1003-1008.
32. J. Zhu, W. Shi, N. Xiao, X. Rui, H. Tan, X. Lu, H. H. Hng, J. Ma and Q. Yan, *ACS Appl Mater Interfaces*, 2012, **4**, 2769-2774.
33. T. c. Chou, R. a. Doong, C. c. Hu, B. Zhang and D. S. Su, *ChemSusChem*, 2014, **7**, 841-847.
34. N. Padmanathan and S. Selladurai, *RSC Adv*, 2014, **4**, 8341-8349.
35. G. Han, Y. Liu, E. Kan, J. Tang, L. Zhang, H. Wang and W. Tang, *RSC Adv*, 2014, **4**, 9898-9904.
36. S. Chen, W. Xing, J. Duan, X. Hu and S. Z. Qiao, *J Mater Chem A*, 2013, **1**, 2941-2954.
37. Y.-F. Li, S.-S. Li, D.-L. Zhou, A.-J. Wang, P.-P. Zhang, C.-G. Li and J.-J. Feng, *J Solid State Electr*, 2014, **18**, 2521-2527.
38. T. Zhu, B. Xia, L. Zhou and X. W. D. Lou, *J Mater Chem*, 2012, **22**, 7851-7855.
39. L. Xie, F. Su, L. Xie, X. Li, Z. Liu, Q. Kong, X. Guo, Y. Zhang, L. Wan and K. Li, *ChemSusChem*, 2015.
40. Z. Fan, J. Yan, T. Wei, L. Zhi, G. Ning, T. Li and F. Wei, *Adv Funct Mater*, 2011, **21**, 2366-2375.
41. L. Qu, Y. Zhao, A. M. Khan, C. Han, K. M. Hercule, M. Yan, X. Liu, W. Chen, D. Wang and Z. Cai, *Nano Lett*, 2015, **15**, 2037-2044.
42. Y.-K. Hsu, Y.-C. Chen, Y.-G. Lin, L.-C. Chen and K.-H. Chen, *Chem Commun*, 2011, **47**, 1252-1254.
43. H. Jang, S. Suzuki and M. Miyayama, *J Electrochem Soc*, 2012, **159**, A1425-A1430.
44. Y.-H. Li, Q.-Y. Li, H.-Q. Wang, Y.-G. Huang, X.-H. Zhang, Q. Wu, H.-Q. Gao and J.-H. Yang, *Appl Energy*, 2014.
45. S. Chen, J. Zhu, X. Wu, Q. Han and X. Wang, *ACS Nano*, 2010, **4**, 2822-2830.
46. Y. Ren, Q. Xu, J. Zhang, H. Yang, B. Wang, D. Yang, J. Hu and Z. Liu, *ACS Appl Mater Interfaces*, 2014, **6**, 9689-9697.
47. H. Wang, C. Peng, F. Peng, H. Yu and J. Yang, *Mater Sci and Eng: B*, 2011, **176**, 1073-1078.
48. A. L. M. Reddy, M. M. Shaijumon, S. R. Gowda and P. M. Ajayan, *J Phys Chem C*, 2009, **114**, 658-663.
49. X. Dong, W. Shen, J. Gu, L. Xiong, Y. Zhu, H. Li and J. Shi, *J Phys Chem B*, 2006, **110**, 6015-6019.
50. J. Zhu and J. He, *ACS Appl Mater Interfaces*, 2012, **4**, 1770-1776.
51. Z. Lei, F. Shi and L. Lu, *ACS Appl Mater Interfaces*, 2012, **4**, 1058-1064.
52. Y. Gao, L. Li, Y. Jin, Y. Wang, C. Yuan, Y. Wei, G. Chen, J. Ge and H. Lu, *Appl Energy*, 2015, **153**, 41-47.

Graphical abstract